Scan-Adaptive MRI Undersampling Using Neighbor-Based Optimization (SUNO)

Siddhant Gautam, *Member, IEEE*, Angqi Li, Nicole Seiberlich, Jeffrey A. Fessler, *Fellow, IEEE*, and Saiprasad Ravishankar, *Senior Member, IEEE*

***Abstract*—Accelerated MRI aims to reduce scan time by acquiring data more efficiently, for example, through optimized pulse sequences or readouts that increase k-space coverage per excitation (e.g., echo planar imaging), or by collecting partial k-space measurements with advanced reconstruction methods. Acceleration via partial k-space acquisition (i.e., undersampling) has received significant attention, particularly with the rise of learning-based reconstruction methods. Recent works have explored population-adaptive sampling patterns learned from groups of patients (or scans), which enhance sampling pattern design by tailoring it to dataset-specific characteristics, rather than relying on generic approaches. Building on this idea, sampling techniques can be further personalized down to the level of individual scans, enabling the capture of subject- or slice-specific details that may be overlooked in population-based designs. To address this challenging problem, we propose a framework for jointly learning scan-adaptive Cartesian undersampling patterns and a corresponding reconstruction model from a training set, enabling more tailored sampling for individual scans. We use an alternating algorithm for learning the sampling patterns and the reconstruction model where we use an iterative coordinate descent (ICD) based offline optimization of scan-adaptive k-space sampling patterns for each example in the training set. A nearest neighbor search is then used to select the scan-adaptive sampling pattern at test time from initially acquired low-frequency k-space information. We applied the proposed framework (dubbed SUNO) to the fastMRI multi-coil knee and brain datasets, demonstrating improved performance over the currently used undersampling patterns at both $4\times$ and $8\times$ acceleration factors in terms of both visual quality and quantitative metrics.**

***Index Terms*—Magnetic resonance imaging, sampling pattern optimization, deep learning, image reconstruction, iterative coordinate descent, nearest neighbor search.**

I. Introduction

MAGNETIC Resonance Imaging (MRI) is a widely used non-invasive biomedical imaging technology that allows visualization of both anatomical structures and physiological functions. Some of its benefits include a lack of ionizing radiation and excellent soft-tissue contrast. MRI scanners sequentially collect measurements in the time (or spatial frequency) domain (known as k-space), from which an image is reconstructed. The scanner must sample numerous k-space points in order to estimate an image with a clinically appropriate spatial resolution, which causes the acquisition process to be slow and expensive. Accelerating MRI scans reduces acquisition time, reduces patient discomfort, increases scanner throughput, and reduces motion artifacts. Such acceleration often requires choosing an appropriate undersampling pattern or trajectory along with a reconstruction model that enables accurate recovery from reduced measurements.

Some of the earliest approaches for accelerating MR imaging included pulse sequence and k-space trajectory design [1], [2], [3] and parallel imaging [4], [5], [6], [7]. Parallel imaging exploits coil sensitivity information but is limited by noise amplification and residual artifacts at higher accelerations. Unlike traditional MRI, which follows the Nyquist–Shannon sampling requirement, compressed sensing (CS) allows sub-Nyquist k-space sampling by exploiting image sparsity in transform domains for accurate reconstruction [8], [9], [10]. Building on this sparsity-driven framework, recent approaches have explored learned image models for reconstruction, including synthesis dictionary learning [11], [12], [13], [14] and transform learning [15], [16].

Over the years, machine learning approaches have been explored for reconstructing MR images from undersampled measurements, including model-driven methods such as ADMM-Net [17], [18] and ISTA-Net [19]. With the advent of deep learning, convolutional neural networks (CNNs) have achieved tremendous success in this task. U-Net architectures [20] trained in a supervised manner have been widely applied for artifact removal [21], [22], [23], [24]. Similarly, variational networks combine neural networks with the MR forward model to address accelerated multi-coil MRI reconstruction [25], [26]. GAN-based methods exploit adversarial learning to improve

Received 1 May 2025; revised 23 September 2025 and 21 December 2025; accepted 29 December 2025. Date of publication 12 January 2026; date of current version 9 March 2026. This work was supported by the National Institutes of Health under Grant R21 EB030762. The associate editor coordinating the review of this article and approving it for publication was Prof. Alejandro F. Frangi. *(Corresponding author: Siddhant Gautam.)*

Siddhant Gautam and Angqi Li are with the Department of Computational Mathematics, Science and Engineering, Michigan State University, East Lansing, MI 48824 USA (e-mail: gautamsi@msu.edu; liangqi1@msu.edu).

Nicole Seiberlich is with the Department of Radiology, University of Michigan, Ann Arbor, MI 48109 USA (e-mail: nse@med.umich.edu).

Jeffrey A. Fessler is with the Department of Electrical Engineering and Computer Science and the Department of Biomedical Engineering, University of Michigan, Ann Arbor, MI 48109 USA (e-mail: fessler@umich.edu).

Saiprasad Ravishankar is with the Department of Computational Mathematics, Science and Engineering and the Department of Biomedical Engineering, Michigan State University, East Lansing, MI 48824 USA (e-mail: ravisha3@msu.edu).

The code for the proposed framework is available at https://github.com/sidgautam95/adaptive-sampling-mri-suno.

This article has supplementary downloadable material available at https://doi.org/10.1109/TCI.2026.3653330, provided by the authors.

Digital Object Identifier 10.1109/TCI.2026.3653330

perceptual quality [27], [28]. More recently, MoDL [29], [30] has become particularly popular, where the MRI forward model is incorporated within a data consistency term and a CNN reconstructor is employed as a learned denoiser to regularize the reconstruction.

Alongside these reconstruction methods, the choice of undersampling pattern is also a crucial aspect to consider. Commonly used undersampling patterns in CS-MRI include variable density [9], uniform random [31], equispaced [32], Poisson-disc [33], and combined variable density and Poisson-disc [34], [35]. Beyond these fixed sampling patterns, early optimization-based approaches aimed to learn undersampling patterns directly from training k-space data by minimizing reconstruction error [36]. Subsequent work on sampling optimization designed adaptive sampling patterns using the power spectra of the reference k-space data [37], [38] or the energy preserving sampling method [39]. Statistical experiment design techniques for MRI sampling prediction were proposed that used the Cramer-Rao lower bound [40], [41]. Later, the greedy algorithm and its variations were used to learn a single population-adaptive sampling pattern over a training set of images with a specific choice of reconstruction method [42], [43]. Since these approaches learn the undersampling pattern using greedy algorithms over a large number of images, the computational cost involved is high, and it scales quadratically with the number of lines in the mask. To avoid this, a stochastic version of the greedy mask learning algorithm was proposed that resolved the scaling issues of the previous greedy approaches [44]. Recently, bias-accelerated subset selection (BASS) [45], [46] was introduced for parallel MRI as a scalable subset-selection method for population-based sampling pattern learning, providing a more efficient alternative to purely greedy approaches.

Deep learning approaches have also been proposed that jointly learn a sampling pattern and a corresponding trained reconstruction network [30], [45], [46], [47], [48], [49], [50], [51], [52]. LOUPE [47] and its multi-coil extension [48] determine the probability of sampling each pixel or row/column in the k-space domain, with the underlying parameters learned jointly with those of the reconstructor (U-Net). Similarly, J-MoDL [30] jointly learns an MoDL reconstruction network and a sampling pattern whose parameters are optimized separately along the row and column directions. More recently, AutoSamp [52] was proposed for joint optimization of sampling patterns and reconstruction in 3D MRI using variational information maximization. These works can be divided into those predicting Cartesian undersampling patterns [45], [46], [47], [50], [51], [52] and those learning non-Cartesian patterns [30]. Other recent works for learning non-Cartesian sampling trajectories include PILOT [53], SPARKLING [54], [55], BJORK [56], NC-PDNet [57], and SNOPY [58].

Sequential decision processes have also been applied to undersampling prediction, where sampling patterns are learned sequentially using reinforcement learning. In these problems, the sampling optimization is formulated as a partially observable Markov decision process (POMDP) [59], [60].

One limitation of the more common population-adaptive approaches [30], [42], [45], [46], [47] is that they learn a single sampling pattern suited to the entire dataset rather than adapting to individual scans. To address this, scan-adaptive undersampling techniques have been proposed that generate sampling patterns individually for each scan by leveraging subject-specific anatomy. For example, SeqMRI [50] trains a reconstruction model jointly with a sampler that predicts sampling patterns sequentially, whereas MNet [51] jointly trains a reconstruction network and a CNN-based sampler to predict undersampling patterns directly from low-frequency k-space data. Such scan-specific approaches can improve reconstruction quality by exploiting key slices or image-specific features, offering potential advantages over conventional population-adaptive techniques. The population-adaptive patterns can be learned offline, whereas scan-specific sampling patterns must be determined rapidly while the subject is in the scanner, after collecting some preliminary k-space data.

This paper proposes a framework for jointly learning scan-adaptive 1D Cartesian undersampling patterns and a reconstruction model for multi-coil MRI on a training dataset. Our algorithm alternatingly estimates a reconstructor and a collection of sampling patterns from training data. We use a sampling optimization algorithm based on iterative coordinate descent to yield improved sampling patterns on training data and use the nearest neighbor search to determine such patterns at test time based on acquired low-frequency k-space. The key methodological difference between the proposed SUNO framework and recent scan-adaptive methods like SeqMRI [50] (or e.g., M-Net [51]) is that the SeqMRI employs a fully differentiable approach, jointly optimizing a sequential sampling policy and a reconstruction strategy via standard backpropagation. In contrast, SUNO formulates mask learning as an integer programming problem and uses a dictionary of learned sampling patterns to find the best mask at test time. Our results show that the scan-adaptive Cartesian sampling patterns yield better reconstruction quality in terms of NRMSE, SSIM [61], and PSNR metrics, compared to existing baselines for multi-coil MRI. This paper builds upon our previous short conference work [62] and extends it to higher acceleration factors and learns undersampling patterns over different anatomies. We also present extended comparisons with several baselines.

The rest of this paper is organized as follows. Section II discusses the details of the MRI forward model, deep learning-based reconstruction, and the details of our proposed training framework that alternates between optimizing a reconstructor and updating scan-adaptive sampling patterns on a training set. Section III discusses the details of training datasets and implementation details. Section IV presents the results of applying our approach to the fastMRI dataset and compares it with existing baselines. We also provide ablation studies on our sampling pattern optimization algorithm. Section V provides a summary of our findings and possible new directions for future work, and further conclusions are provided in Section VI.

II. Methods

A. Multi-Coil MRI Reconstruction

In multi-coil MRI reconstruction, the goal is to recover the underlying MR image $\mathbf{x} \in \mathbb{C}^n$ from a set of undersampled

multi-coil measurements $\mathbf{y} \in \mathbb{C}^m$. The regularized MRI reconstruction problem can be formulated as follows:

$$\min_{\mathbf{x}} \|\mathbf{MAx} - \mathbf{y}\|_2^2 + \lambda \mathcal{R}(\mathbf{x}) \tag{1}$$

Here, $\mathbf{M}$ is an operator that subsamples k-space, $\mathbf{A} = \mathbf{FS}$ is the fully sampled MRI measurement operator and $\mathcal{R}(\mathbf{x})$ is a regularizer. $\mathbf{F}$ is the 2D Fourier transform operator and $\mathbf{S}$ encodes the sensitivity maps of the receiver coils. The regularizer $\mathcal{R}(\mathbf{x})$ typically captures assumed properties of the image and can take on various forms such as total variation, or low-rank or transform-domain sparsity penalties.

Recently, deep learning has become an increasingly powerful tool for MRI reconstruction, eliminating the need for hand-crafted regularizers. In this paper, we discuss four such approaches: U-Net [20], [21], MoDL [29], VarNet [25], [26], and ZS-SSL [63]. U-Net [20] is a convolutional encoder–decoder that predicts the underlying clean image directly from the aliased input. Building on this, model-based deep learning (MoDL) [29] adopts a fully unrolled, end-to-end trainable framework that alternates between data consistency enforced via the MR forward model and CNN-based denoising, formulated as

$$\hat{\mathbf{x}} = \arg\min_{\mathbf{x}} \|\mathbf{MAx} - \mathbf{y}\|_2^2 + \lambda \|\mathbf{x} - D_{\boldsymbol{\theta}}(\mathbf{x})\|_2^2, \tag{2}$$

where $D_{\boldsymbol{\theta}}(\mathbf{x})$ is a CNN denoiser with parameters $\boldsymbol{\theta}$. Variational networks [25] follow a similar approach, alternating between the k-space data consistency and CNN-based image-domain priors. End-to-end VarNet (E2E-VarNet) [26] further extends this approach by fully unrolling the reconstruction process and incorporating k-space domain processing, achieving state-of-the-art performance in multi-coil MRI. Finally, Zero-Shot Self-Supervised Learning (ZS-SSL) [63] trains a network directly on undersampled measurements from individual scans by partitioning k-space into disjoint sets for training, self-supervision, and validation, enabling scan-specific reconstructions without fully sampled references.

In this paper, we focus on learning scan-specific sampling patterns $\{\mathbf{M}_i\}$ instead of a single population-adaptive sampling pattern. In this framework, we first optimize these scan-adaptive masks $\{\mathbf{M}_i\}$ offline for the training set. Then at test time, these masks are chosen using a nearest neighbor search, as described in a later subsection. Fig. 1 shows the scan adaptive sampling patterns learned by the proposed sampling optimization framework. The optimized patterns consistently sample the k-space center across subjects, whereas the high-frequency lines vary depending on the anatomy of the scan and the coil sensitivities, reflecting the scan-adaptive nature of the approach.

B. Framework for Jointly Learning Reconstructor and Sampler

This section presents our proposed approach for jointly learning a set of scan-adaptive Cartesian undersampling patterns $\{\mathbf{M}_i\}$ along with a reconstructor trained to be suitable for all of these undersampling patterns. Using a training set consisting of fully sampled k-space and corresponding ground truth images, we learn a collection of scan-adaptive sampling masks and a reconstructor from the training data. We formulated the joint

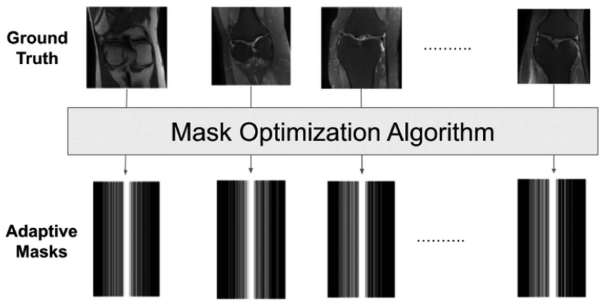

Fig. 1. Illustration of scan-adaptive undersampling patterns generated by our proposed sampling optimization framework. Central k-space is consistently sampled across cases, while the high frequency lines vary across the subjects, reflecting individual anatomy and coil sensitivity profiles.

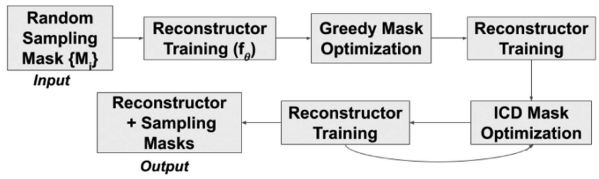

Fig. 2. Alternating framework for mask and reconstructor update during joint training. The first four steps serve to create a good initialization for the mask and reconstructor optimization. The masks could be alternatively initialized with, e.g., population-adapted patterns.

optimization problem as follows:

$$\min_{\boldsymbol{\theta},\, \mathbf{M}_i \in \mathcal{C},\, i \in \{1,\ldots,N\}} \sum_{i=1}^{N} \|f_{\boldsymbol{\theta}}(\mathbf{A}_i^H \mathbf{M}_i \mathbf{y}_i^{\text{full}}) - \mathbf{x}_i^{\text{gt}}\|_2^2, \tag{3}$$

where $\mathbf{M}_i \in \mathcal{C}$ is the ith training k-space subsampling mask that inserts zeros at non-sampled locations, $\mathbf{y}_i^{\text{full}}$ and $\mathbf{x}_i^{\text{gt}}$ are the ith fully sampled multi-coil training k-space and the corresponding ground truth image, respectively and N is the number of training images. The set $\mathcal{C}$ denotes all the 1D Cartesian undersampling patterns with a specified sampling budget. $\mathbf{A}_i^H$ is the adjoint of the fully sampled multi-coil MRI measurement operator for the ith training scan, and $f_{\boldsymbol{\theta}}$ is the reconstruction network trained on the set of sampling patterns $\{\mathbf{M}_i\}$.

We use the alternating framework shown in Fig. 2 to solve this highly challenging optimization problem. The algorithm starts with random masks as an initial guess [9] and alternates between updating a reconstructor and sampling masks until we get a final set of scan-adaptive masks $\{\mathbf{M}_i\}$ and a reconstruction network $f_{\boldsymbol{\theta}}$ trained on them. For optimizing the scan-adaptive masks, we initially use a greedy [42] and later our proposed ICD-based sampling optimization algorithm. More details of the sampling optimization algorithm are in the next section.

C. Iterative Coordinate Descent (ICD) Based Sampling Optimization

A greedy algorithm was proposed in prior work [42] to optimize high-quality sampling patterns that specify samples in k-space that minimize the reconstruction error given a choice of the reconstruction model used. Starting with no sampled lines

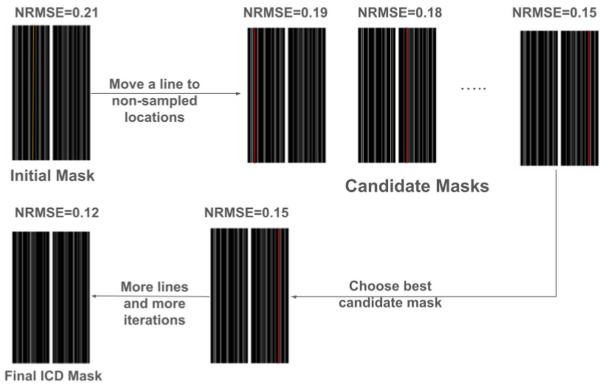

Fig. 3. Schematic of offline iterative coordinate descent (ICD) based sampling pattern optimization.

or only fixed low-frequency lines, at each step of the greedy sampling optimization, the k-space phase encoding line that gives the lowest reconstruction error is added to a particular sampling mask. The algorithm keeps adding lines until the sampling budget is reached. However, the sampling pattern obtained using the greedy algorithm can be sub-optimal and can be further optimized using an iterative coordinate descent (ICD) based sampling optimization. The proposed iterative coordinate descent (ICD) based sampling optimization algorithm further optimizes the greedy mask iteratively by picking one line at a time in the current mask and moving it to the best new location in terms of the reconstruction error, and cycling over all lines to move in this manner. Fig. 3 shows the schematic of mask updates during various steps of the ICD sampling optimization. The steps of the algorithm are given in detail in Algorithm 1. Thus, the ICD sampling optimization further improves the greedy masks and yields better quality scan-adaptive masks. The optimized masks depend on the choice of the initial mask, the reconstructor used, and the metric chosen for the loss function. The ICD sampling optimization algorithm ensures a monotonic decrease and convergence of the non-negative reconstruction loss (3).

D. Neighbor Based Sampling Prediction

This subsection describes our approach to predict the sampling pattern from initially acquired k-space measurements at testing time. Given our set of scan-adaptive sampling patterns obtained from the training process, the task at test time is to estimate the high-frequency lines in k-space based on initially acquired low-frequency information. We use the nearest neighbor search to predict the sampling pattern from the collection of training scans. The nearest neighbor is found by comparing the adjoint reconstruction of the low-frequency test k-space and the corresponding low-frequency part of the training k-space as follows:

$$d_i = d(\mathbf{A}_{\text{test}}^H \mathbf{y}_{\text{test}}^{\text{lf}}, \mathbf{A}_{\text{train}_i}^H \mathbf{y}_{\text{train}_i}^{\text{lf}}), \tag{4}$$

where $\mathbf{y}_{\text{test}}^{\text{lf}}$ and $\mathbf{y}_{\text{train}_i}^{\text{lf}}$ are the low-frequency part of testing and training k-space with zeros at high frequencies. $\mathbf{A}_{\text{test}}^H$ and $\mathbf{A}_{\text{train}_i}^H$ are the adjoints of the fully sampled MRI forward operators for the test and ith training scans, respectively. Different metrics d can be used to define the nearest neighbors, e.g., Euclidean distance, structural similarity index (SSIM) [61], or normalized cross-correlation. In this work, we used the Euclidean distance between the zero-filled reconstructions obtained from the low-frequency k-space data to identify the nearest neighbor. We choose the optimized mask of the nearest neighbor (called the SUNO mask) and use that at test time in the scanner to collect the rest of the measurements.

Algorithm 1: Sampling Pattern Optimization.

Require: Fully sampled k-space $\mathbf{y}^{\text{full}}$ and corresponding forward operator $\mathbf{A}$, ground truth image $\mathbf{x}^{\text{gt}}$, reconstructor f, loss function L, budget B, number of ICD iterations N_{iter}, set of all possible line locations $\mathbf{S}$, set of locations of initial sampled lines $\mathbf{\Omega}_{\text{initial}}$, initial mask $\mathbf{M}_{\mathbf{\Omega}_{\text{initial}}}$

$\mathbf{\Omega} \leftarrow \mathbf{\Omega}_{initial}$
for $j = 1 : N_{\text{iter}}$ **do**
  $\{l_i\}_{i=1}^{B} \leftarrow$ entries in current $\mathbf{\Omega}$
  for $i = 1 : B$ **do**
    $\mathbf{\Omega}' = \mathbf{\Omega} \setminus l_i$
    $\mathbf{\Omega} \leftarrow \mathbf{\Omega}' \cup S^*$ where

$$S^* = \underset{S \in \mathbf{S},\, S \notin \mathbf{\Omega}'}{\arg\min}\; L(\mathbf{x}^{\text{gt}}, f(\mathbf{A}^H \mathbf{M}_{\mathbf{\Omega}' \cup S} \mathbf{y}^{\text{full}}))$$

    where $\mathbf{M}_{\mathbf{\Omega}' \cup S}$ is the operator sampling along lines at $\mathbf{\Omega}' \cup S$.
  end for
end for
return $\mathbf{\Omega}$

III. Experiments

A. Datasets

Our experiments used the fastMRI multi-coil knee and brain datasets [64], [65]. The details for each dataset are as follows:

1) fastMRI Multi-Coil Knee Dataset: The fastMRI multi-coil knee dataset contains images collected using two different pulse sequences, yielding coronal proton-density weighted images with (PDFS) and without (PD) fat suppression. For our experiments, we used a total of 156 scans (comprising both PD and PDFS scans) and split them into training, validation, and testing sets. From each scan, we discarded the first 10 and last 5 slices due to a lack of identifiable image features, which gave us 1514, 194, and 104 training, validation, and testing slices, respectively. Each image was collected using 15 coils of k-space data with a matrix size of 640×368. We used the ESPIRIT calibration approach [4], [66] to estimate the sensitivity maps from the central 30 lines of k-space.

2) fastMRI Multi-Coil Brain Dataset: To test the generalization of our proposed sampling prediction algorithm, we also applied our algorithm on the fastMRI multi-coil brain dataset which consists of FLAIR, T1-weighted, and T2-weighted images. From this dataset, we used a total of 1660 slices for our experiments and split them into 1480, 120, and 60 training, validation, and testing images, respectively. The scans were acquired with a matrix acquisition size of 640×320, and the

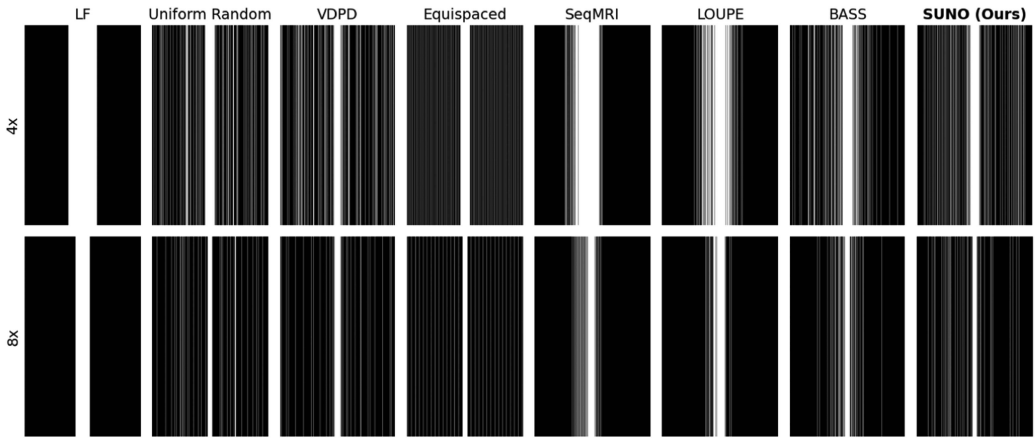

Fig. 4. Comparison of different masks used for reconstruction at a) $4\times$ and b) $8\times$ acceleration factors for the knee dataset. Masks displayed are: 1) low-frequency (fixed), 2) 1D Uniform Random (random), 3) VDPD (random), 4) Equispaced (fixed), 5) SeqMRI (optimized - scan adaptive), 6) LOUPE (optimized - population adaptive), 7) BASS (optimized - population adaptive), and 8) SUNO (optimized - scan adaptive). For the scan-adaptive methods (SeqMRI and SUNO), only one representative mask is shown here for each acceleration factor; additional instances illustrating variability are provided in the supplementary document.

number of receiver coils varied between 4 and 20 across different scans. The sensitivity maps were estimated using the ESPIRiT calibration approach.

B. Comparison With Other Undersampling Patterns

We compared our proposed SUNO sampling patterns with several baselines. Classical baselines included low-frequency (LF), uniform random [31], equispaced [32], and variable-density Poisson-disc (VDPD) [33], [35] masks. Learned baselines included scan-adaptive SeqMRI [50], population-adaptive LOUPE [47], and BASS [45], [46] (all Cartesian). All methods were adapted for 1D Cartesian sampling along the phase-encoding (k_y) direction for clinical 2D MRI.

For SeqMRI and LOUPE, we used their publicly available PyTorch implementations [1] and extended them to the multi-coil setting. In LOUPE, the slope parameter was set to $\alpha = 5$, with a learning rate of 10^{-3} for mask updates. SeqMRI was trained with a learning rate of 5×10^{-5}, halved every 10 epochs, with four sequential steps and an SSIM loss between real-valued magnitude-only images. For reconstruction, LOUPE used a two-channel U-Net, while SeqMRI used a two-channel residual U-Net; both networks started with 64 channels and were trained for 100 epochs. For each undersampling pattern, 30 and 15 central low-frequency lines were fixed for $4\times$ and $8\times$ acceleration, respectively. In our experiments, the learned LOUPE masks at $4\times$ and $8\times$ accelerations showed different sampling distributions compared to their prior work [47]. These differences can be partly due to our use of a multi-coil MRI setup with a larger matrix size (640×368) compared to their original single-coil study with a smaller matrix size (320×320). Additionally, in our implementation, we incorporated a straight-through (ST) estimator [67] for binary mask generation during training, similar to the approach used in the multi-coil extension of LOUPE [48].

For obtaining the BASS mask, we used the MATLAB implementation available at the authors' website.[2] We followed the default settings in the released code, and used the sampling pattern (SP) learning parameter $\alpha = 0.9$ in the 1D SP mode. As with the other baselines, K_{LF} central lines were fixed for calibration for each acceleration factor. The algorithm was run for $L = 100$ iterations for both cases. Similar to the LOUPE setting, the BASS mask was optimized over the whole training set. Separate masks were optimized on the brain dataset at acceleration factors of $4\times$ and $8\times$.

All reconstruction models (ZS-SSL, E2E-VarNet, MoDL) were retrained separately for every mask setting, including population-adaptive masks such as BASS, to ensure fair and consistent comparisons across all methods. Fig. 4 shows representative SUNO and baseline masks for the knee dataset. Here we adapted the VDPD approach [35] to 1D Cartesian undersampling along the phase-encoding direction for a fair comparison with our learned masks. Although the VDPD masks are adapted for 1D Cartesian undersampling along the phase-encoding direction, they still follow the Poisson-disc principle with enforced minimum spacing. In 1D, the variable-density pattern can visually resemble a uniform random mask, but the underlying sampling distribution is different; these differences become more apparent in 2D sampling.

Table I lists the parameters used in the sampling optimization algorithm for each acceleration factor. The number of ICD iterations T was set to 1, as most of the loss reduction occurs in the first iteration, while additional iterations provide marginal improvements at higher computational cost.

C. Implementation Details

Our algorithms were implemented in Python, using the PyTorch package. We used two-channel reconstruction networks to obtain the underlying image from the undersampled k-space, with the two channels being the real and imaginary parts of the complex image. We used Facebook Research's implementation

[1]https://github.com/tianweiy/SeqMRI; https://github.com/cagladbahadir/LOUPE

[2]https://cai2r.net/resources/data-driven-learning-of-mri-sampling-pattern/

TABLE I
PARAMETERS INVOLVED IN THE ICD SAMPLING OPTIMIZATION ALGORITHM FOR THE FASTMRI MULTI-COIL KNEE DATASET WITH k-SPACE DIMENSION $N_x \times N_y$, WHERE $N_x = 640$ AND $N_y = 368$. ONE-THIRD OF THE SAMPLED LINES ARE FIXED AT THE CENTER OF k-SPACE (c), AND THE REMAINING $m = B - c$ LINES ARE OPTIMIZED BY THE ALGORITHM. THE CANDIDATE SEARCH SPACE FOR EACH UPDATE IS $(N_y - B)$. FOR THE BRAIN DATASET, THE PARAMETERS SCALE ACCORDINGLY WITH THE DATASET MATRIX SIZE.

Acceleration Factor	**4×**	**8×**
Total sampled lines (B)	92	46
Centrally fixed lines (c)	30	15
Lines updated by ICD ($m = B - c$)	62	31
Candidate search space ($N_y - B$)	276	322
No. of ICD iterations (N_{iter})	1	1

of U-Net in the PyTorch framework[3]. For MoDL [29], we used a deep iterative up-down (DIDN) network [68] as the denoiser inside the training framework. We used 6 unrollings of the denoiser and the conjugate gradient (CG) block. The regularization parameter λ controlling the weighting of the two terms (see Eq.(2)) was set to 10^2 and the tolerance for the CG algorithm used was 10^{-5} after tuning them on multiple images. For VarNet [26], we used 12 cascades, each containing a U-Net with 18 channels in the first layer, using the official implementation provided by Facebook Research.[4] Sensitivity maps used for VarNet training were estimated using the ESPIRIT calibration approach [66]. The reconstructed image was obtained by applying the adjoint of the forward MRI operator to the reconstructed k-space from VarNet. Both MoDL and VarNet were trained for 100 epochs with a batch size of 1. Adam optimizer [69] was used for training the networks with a learning rate of 10^{-3}. For the ZS-SSL approach [63], we employed 10 unrolled blocks and 15 residual blocks, along with 10 conjugate gradient iterations for data consistency. The model was trained for 300 epochs with a learning rate of 5×10^{-4} using the official implementation available on GitHub.[5] The simulations were performed on an NVIDIA RTX A5000 GPU with 24 GB RAM.

D. Performance Metrics

To evaluate the quality of reconstructed images, we used normalized root mean squared error (NRMSE), structural similarity index measure (SSIM) [61], and peak signal-to-noise ratio (PSNR) as the metrics. These metrics assess the similarity between the ground truth and the reconstructed images. Lower NRMSE, higher SSIM, and PSNR values suggest better reconstruction quality. All the metrics were evaluated on the central 320×320 portion of the image.

IV. RESULTS

A. Studies on the fastMRI Multi-Coil Knee Dataset

In this section, we show the result of applying our optimized scan-adaptive SUNO masks on the fastMRI multi-coil knee dataset at $4\times$ and $8\times$ acceleration factors. We compare the quality of the reconstructed images using our optimized masks with the other baseline masks described in Section III-B.

Fig. 5 shows the images reconstructed using the MoDL network (along with zoom-ins over a region of interest) at $4\times$ acceleration. It is clear from the figure that the proposed SUNO provides better-reconstructed images compared to other baselines in terms of NRMSE, SSIM, and PSNR metrics. The zoom-ins also show that the reconstructed image using the SUNO mask preserves fine structural details present in the ground truth. Fig. 6 shows reconstructed and error images at $8\times$ acceleration using the SUNO along with other baselines. The error maps indicate that BASS yields the best quality reconstruction, with SUNO giving comparable reconstructions.

Table II reports the mean and standard deviation values of NRMSE, SSIM, and PSNR for reconstructed images using ZS-SSL [63], E2E-VarNet [26], and MoDL [29]. On average, the proposed SUNO outperformed most baselines across different acceleration factors and reconstructors. At $4\times$ acceleration, SUNO achieved the best performance with both VarNet and MoDL. However, at $8\times$ acceleration, the BASS mask performed comparably to, and in some cases slightly better than SUNO for VarNet and MoDL. For the ZS-SSL reconstruction method, SUNO gave the best performance in terms of the reconstruction metrics at both $4\times$ and $8\times$ acceleration factors.

B. Applicability to Different Anatomies

To test the applicability of our proposed scan-adaptive sampling prediction approach on different anatomies, we also optimized masks using the proposed training pipeline on the fastMRI multi-coil brain dataset. Then, using the nearest neighbor search, the masks were predicted at test time, and the performance of these learned SUNO masks was compared with the other baselines - low-frequency, Uniform Random, equispaced, SeqMRI, and LOUPE masks.

Figs. 7 and 8 show the reconstructed and error images using a brain testing slice for $4\times$ and $8\times$ acceleration factors. The figure shows that the optimized scan adaptive SUNO masks outperform the other baseline masks in terms of the reconstruction metrics for both $4\times$ and $8\times$ acceleration factors. The error images indicate a lower reconstruction error for SUNO approach. The mean and standard deviation values of the reconstruction metrics using ZS-SSL, VarNet, and MoDL reconstruction methods learned over all test cases are mentioned in Table III. From the table, we can see that the proposed SUNO approach outperformed all baselines for all three reconstruction approaches in terms of the error metrics used.

C. Comparison With the Oracle Case

In this section, we compare the performance of oracle masks optimized directly on the test slices (using the sampling optimization with a fixed reconstructor) with the ones predicted from the nearest neighbor search (SUNO masks). Table IV gives a comparison of the oracle and SUNO masks for the fastMRI knee dataset. We observe that the oracle-optimized masks perform better than the SUNO mask for both acceleration factors, as expected. This is because the oracle mask was optimized for the

[3]https://github.com/facebookresearch/fastMRI/blob/main/fastmri/models/unet.py
[4]https://github.com/facebookresearch/fastMRI/blob/main/fastmri/models/varnet.py
[5]https://github.com/byaman14/ZS-SSL-PyTorch

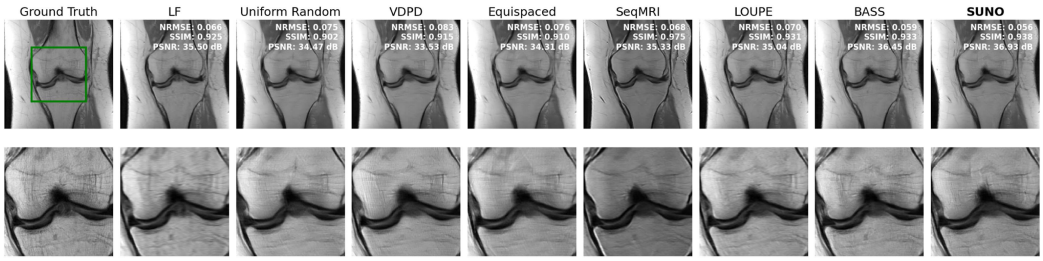

Fig. 5. Reconstructed images using MoDL reconstruction network at $4\times$ acceleration factor for a testing slice. The second row shows the zoom-in images from the area inside the green rectangle. The SUNO approach outperformed the rest in terms of visual quality and better preserved structural detail, whereas BASS offered similar performance.

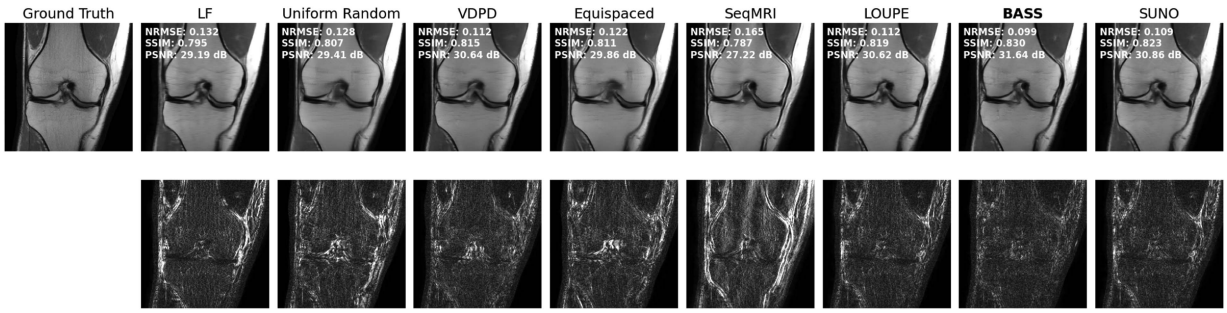

Fig. 6. Reconstructed images using MoDL reconstruction network at $8\times$ acceleration factor with the error maps in the second row. At $8\times$, the population-adaptive BASS mask achieved the lowest reconstruction error and best preserved structural details, while SUNO still provided competitive reconstructions. The error images (magnitudes) are shown in the range $[0,\ 0.1]$.

TABLE II

DISTRIBUTION OF NRMSE, SSIM, AND PSNR VALUES FOR RECONSTRUCTED IMAGES FROM THE MULTICOIL KNEE DATASET AT $4\times$ AND $8\times$ ACCELERATION FACTORS. FOR ZS-SSL, SUNO ACHIEVED THE BEST PERFORMANCE AT BOTH $4\times$ AND $8\times$ ACCELERATION. FOR E2E-VARNET AND MODL, SUNO PERFORMED BEST AT $4\times$ ACCELERATION. AT $8\times$ ACCELERATION, THE POPULATION-ADAPTIVE BASS MASK ACHIEVED THE LOWEST NRMSE AND HIGHEST SSIM FOR E2E-VARNET AND MODL, INDICATING THAT A SINGLE GLOBAL MASK CAN PROVIDE STABILITY UNDER EXTREME UNDERSAMPLING, WHILE SUNO REMAINED COMPETITIVE.

Reconstructor	Mask	$4\times$			$8\times$		
		NRMSE ↓	SSIM ↑	PSNR (dB) ↑	NRMSE ↓	SSIM ↑	PSNR (dB) ↑
ZS-SSL [63]	LF	0.156 ± 0.074	0.794 ± 0.072	29.15 ± 2.80	0.260 ± 0.100	0.690 ± 0.090	24.90 ± 3.20
	Uniform Random	0.125 ± 0.052	0.834 ± 0.074	30.94 ± 2.87	0.235 ± 0.095	0.700 ± 0.085	25.50 ± 3.00
	VDPD [33], [35]	0.123 ± 0.060	0.832 ± 0.083	31.30 ± 3.40	0.200 ± 0.095	0.730 ± 0.095	27.20 ± 3.00
	Equispaced [32]	0.117 ± 0.053	0.841 ± 0.070	31.62 ± 2.94	0.232 ± 0.107	0.705 ± 0.085	25.64 ± 2.82
	SeqMRI [50]	0.118 ± 0.040	0.846 ± 0.081	31.56 ± 2.89	0.199 ± 0.113	0.732 ± 0.118	27.12 ± 3.42
	LOUPE [47]	0.119 ± 0.057	0.848 ± 0.071	31.54 ± 3.22	0.193 ± 0.112	0.746 ± 0.102	27.67 ± 3.48
	BASS [45], [46]	0.113 ± 0.060	0.840 ± 0.089	32.20 ± 3.40	0.195 ± 0.100	0.740 ± 0.090	27.30 ± 3.10
	SUNO (Ours)	**0.110 ± 0.058**	**0.860 ± 0.081**	**32.38 ± 3.43**	**0.192 ± 0.116**	**0.746 ± 0.104**	**27.69 ± 3.50**
E2E-VarNet [26]	LF	0.133 ± 0.059	0.866 ± 0.052	30.50 ± 2.77	0.194 ± 0.114	0.783 ± 0.071	27.55 ± 3.07
	Uniform Random	0.127 ± 0.053	0.864 ± 0.055	30.79 ± 2.74	0.186 ± 0.064	0.801 ± 0.065	27.67 ± 2.49
	VDPD [33], [35]	0.121 ± 0.050	0.869 ± 0.055	31.25 ± 2.78	0.151 ± 0.060	0.817 ± 0.068	29.31 ± 2.63
	Equispaced [32]	0.118 ± 0.046	0.873 ± 0.054	31.56 ± 2.76	0.182 ± 0.061	0.812 ± 0.059	27.86 ± 2.33
	SeqMRI [50]	0.117 ± 0.052	0.892 ± 0.052	31.58 ± 2.81	0.155 ± 0.054	0.833 ± 0.062	28.90 ± 2.35
	LOUPE [47]	0.113 ± 0.051	0.890 ± 0.051	32.00 ± 2.90	0.148 ± 0.064	0.828 ± 0.065	29.51 ± 2.66
	BASS [45], [46]	0.108 ± 0.050	0.890 ± 0.053	32.48 ± 2.99	**0.140 ± 0.061**	**0.843 ± 0.063**	**29.99 ± 2.62**
	SUNO (Ours)	**0.107 ± 0.051**	**0.896 ± 0.053**	**32.55 ± 3.11**	0.147 ± 0.062	0.828 ± 0.065	29.57 ± 2.62
MoDL [29]	LF	0.134 ± 0.066	0.929 ± 0.031	30.59 ± 3.05	0.187 ± 0.094	0.781 ± 0.071	27.67 ± 2.83
	Uniform Random	0.137 ± 0.051	0.920 ± 0.031	31.08 ± 2.50	0.198 ± 0.065	0.759 ± 0.068	26.76 ± 2.26
	VDPD [33], [35]	0.131 ± 0.049	0.846 ± 0.055	30.45 ± 2.85	0.164 ± 0.064	0.788 ± 0.070	28.49 ± 2.63
	Equispaced [32]	0.127 ± 0.050	0.927 ± 0.031	30.67 ± 2.58	0.190 ± 0.067	0.766 ± 0.070	27.56 ± 2.27
	SeqMRI [50]	0.118 ± 0.048	0.939 ± 0.028	31.50 ± 2.79	0.170 ± 0.058	0.790 ± 0.062	26.30 ± 2.09
	LOUPE [47]	0.116 ± 0.049	0.938 ± 0.028	31.63 ± 2.81	0.163 ± 0.072	0.804 ± 0.067	28.56 ± 2.78
	BASS [45], [46]	0.115 ± 0.049	0.867 ± 0.055	31.67 ± 2.80	**0.155 ± 0.061**	**0.805 ± 0.065**	**28.99 ± 2.44**
	SUNO (Ours)	**0.114 ± 0.046**	**0.940 ± 0.029**	**31.74 ± 2.85**	0.162 ± 0.065	0.801 ± 0.068	28.66 ± 2.61

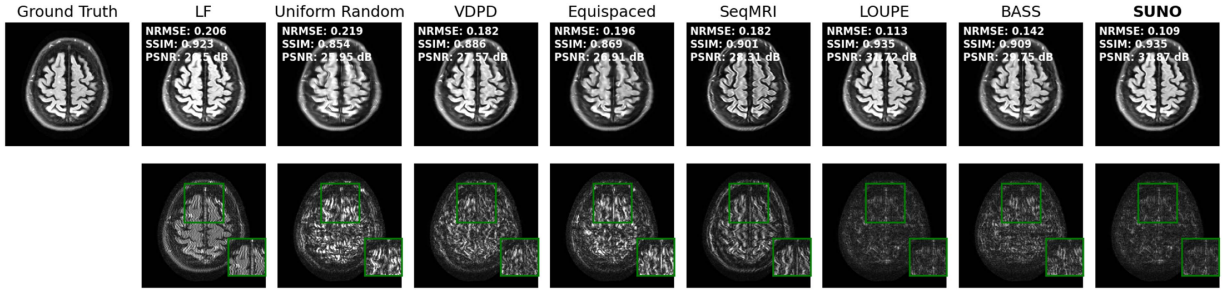

Fig. 7. Reconstructed and error images using different undersampling patterns with the MoDL reconstruction network (two-channel) on the fastMRI brain dataset at $4\times$ acceleration. The green rectangle highlights the zoomed-in regions in the error images. The proposed SUNO achieved the best performance in terms of NRMSE and PSNR, while obtaining SSIM comparable to LOUPE.

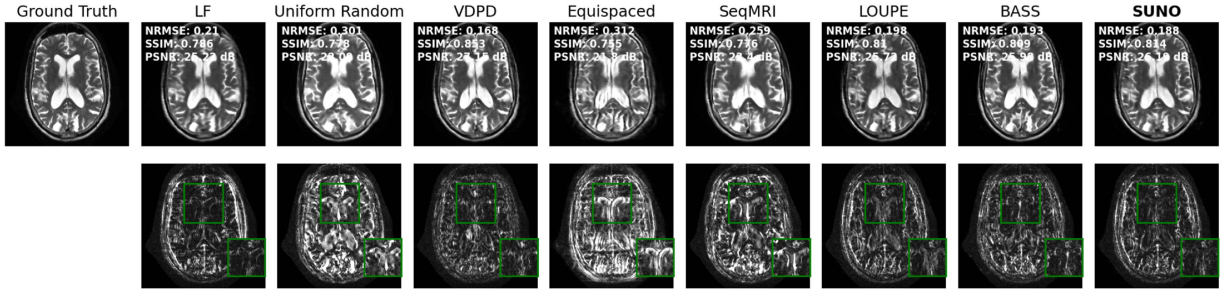

Fig. 8. Reconstructed and error images using different undersampling patterns using MoDL reconstruction network(two-channel) on fastMRI brain dataset at $8\times$ acceleration factor. The green rectangle shows the zoomed-in portions in the error image. The proposed SUNO performed better than other baselines in terms of NRMSE, SSIM, and PSNR metrics.

TABLE III

DISTRIBUTION OF NRMSE, SSIM, AND PSNR VALUES FOR THE RECONSTRUCTED IMAGES FROM THE MULTICOIL BRAIN DATASET AT $4\times$ AND $8\times$ ACCELERATION FACTORS USING VARIOUS MASKS AND RECONSTRUCTORS. THE SUNO OUTPERFORMS THE REST AT BOTH ACCELERATION FACTORS FOR ALL THREE RECONSTRUCTION METHODS USED. THE VALUES DISPLAYED ARE MEAN $\pm$ STD.

		$4\times$			$8\times$		
Reconstructor	Mask	NRMSE ↓	SSIM ↑	PSNR (dB) ↑	NRMSE ↓	SSIM ↑	PSNR (dB) ↑
ZS-SSL [63]	LF	0.173 ± 0.057	0.854 ± 0.025	29.14 ± 2.46	0.259 ± 0.067	0.764 ± 0.046	25.45 ± 2.14
	Uniform Random	0.124 ± 0.034	0.873 ± 0.029	31.83 ± 2.50	0.241 ± 0.065	0.802 ± 0.061	26.07 ± 2.37
	VDPD [33], [35]	0.123 ± 0.033	0.896 ± 0.027	32.02 ± 2.40	0.247 ± 0.056	0.840 ± 0.027	25.59 ± 1.17
	Equispaced [32]	0.120 ± 0.032	0.891 ± 0.028	32.13 ± 2.30	0.297 ± 0.053	0.742 ± 0.049	24.09 ± 1.36
	SeqMRI [50]	0.118 ± 0.027	0.897 ± 0.025	32.22 ± 2.76	0.171 ± 0.060	0.841 ± 0.029	27.98 ± 2.06
	LOUPE [47]	0.114 ± 0.024	0.900 ± 0.021	32.61 ± 2.20	0.166 ± 0.037	0.864 ± 0.025	28.94 ± 1.93
	BASS [45], [46]	0.119 ± 0.031	0.892 ± 0.026	32.18 ± 2.18	0.161 ± 0.057	0.864 ± 0.029	29.12 ± 1.93
	SUNO (Ours)	**0.111 ± 0.025**	**0.903 ± 0.020**	**32.83 ± 2.02**	**0.158 ± 0.040**	**0.869 ± 0.024**	**29.35 ± 1.92**
E2E-VarNet [26]	LF	0.144 ± 0.047	0.964 ± 0.012	30.74 ± 2.63	0.216 ± 0.064	0.881 ± 0.035	27.03 ± 2.38
	Uniform Random	0.116 ± 0.025	0.970 ± 0.010	32.37 ± 1.89	0.196 ± 0.040	0.889 ± 0.029	27.72 ± 1.73
	VDPD [33], [35]	0.110 ± 0.021	0.946 ± 0.013	32.58 ± 1.66	0.208 ± 0.043	0.880 ± 0.026	27.18 ± 1.74
	Equispaced [32]	0.118 ± 0.022	0.970 ± 0.009	32.20 ± 1.64	0.171 ± 0.044	0.923 ± 0.021	28.92 ± 2.12
	SeqMRI [50]	0.109 ± 0.026	0.973 ± 0.008	33.01 ± 2.09	0.172 ± 0.044	0.920 ± 0.019	28.91 ± 1.94
	LOUPE [47]	0.104 ± 0.024	0.978 ± 0.006	33.40 ± 2.09	0.165 ± 0.037	0.910 ± 0.022	29.24 ± 1.63
	BASS [45], [46]	0.115 ± 0.023	0.958 ± 0.012	33.35 ± 2.12	0.167 ± 0.040	0.908 ± 0.017	29.15 ± 2.10
	SUNO (Ours)	**0.102 ± 0.023**	**0.978 ± 0.006**	**33.51 ± 2.09**	**0.162 ± 0.044**	**0.922 ± 0.020**	**29.51 ± 2.08**
MoDL [29]	LF	0.154 ± 0.046	0.956 ± 0.014	30.22 ± 2.57	0.239 ± 0.073	0.843 ± 0.036	26.17 ± 2.21
	Uniform Random	0.175 ± 0.052	0.938 ± 0.019	29.28 ± 2.20	0.252 ± 0.058	0.827 ± 0.036	25.57 ± 1.75
	VDPD [33], [35]	0.158 ± 0.036	0.896 ± 0.018	29.77 ± 2.05	0.250 ± 0.055	0.830 ± 0.034	25.70 ± 1.78
	Equispaced [32]	0.156 ± 0.038	0.941 ± 0.020	29.93 ± 2.01	0.257 ± 0.056	0.823 ± 0.035	25.38 ± 1.84
	SeqMRI [50]	0.122 ± 0.035	0.958 ± 0.017	31.87 ± 2.15	0.204 ± 0.068	0.828 ± 0.034	27.34 ± 1.57
	LOUPE [47]	0.119 ± 0.033	0.931 ± 0.014	32.38 ± 2.26	0.192 ± 0.055	0.870 ± 0.029	28.12 ± 2.07
	BASS [45], [46]	0.124 ± 0.031	0.921 ± 0.025	31.92 ± 2.20	0.202 ± 0.057	0.864 ± 0.029	27.58 ± 1.93
	SUNO (Ours)	**0.117 ± 0.031**	**0.962 ± 0.013**	**32.54 ± 2.20**	**0.191 ± 0.058**	**0.871 ± 0.029**	**28.16 ± 2.11**

TABLE IV
COMPARISON OF THE ORACLE AND SUNO MASKS ON THE FASTMRI KNEE DATASET TEST CASES. VALUES ARE REPORTED AS MEAN NRMSE / SSIM / PSNR.

Acceleration Factor	4×	8×
Oracle	**0.111 / 0.942 / 31.87**	**0.149 / 0.902 / 29.60**
SUNO	0.114 / 0.940 / 31.74	0.162 / 0.801 / 28.66

particular test scan (scan-adaptive) while the SUNO mask uses the mask optimized on the nearest neighbor training scan. Hence, the oracle masks perform slightly better in general. However, we want to emphasize that estimating the oracle masks requires access to the ground truth, making it infeasible at test time.

D. Effect of Local Neighbor-Adaptive Reconstruction

In this subsection, we evaluate the effect of combining the proposed scan-adaptive SUNO approach with a local neighbor-adaptive reconstruction technique [70]. Adaptive local network training on a small set of nearest neighbors has been shown to improve reconstruction quality compared to globally trained models, particularly when the local training data closely resemble the test image [70]. By focusing on a small, relevant subset of scans, the reconstruction network can better adapt to shared image features while avoiding the variability present in large, heterogeneous training sets.

We refer to this setting as SUNO-Local, which uses local neighbor-adaptive reconstruction, and compare it with SUNO-Global, where reconstruction is performed using a globally trained MoDL network. For both settings, the SUNO mask for each test scan is selected using the nearest-neighbor search described in Section II.

For the local training configuration, the MoDL reconstruction network is initialized from the globally trained model and fine-tuned using the 30 nearest-neighbor training scans for 50 epochs. A reduced learning rate of 10^{-6} is used to mitigate overfitting due to the limited size of the local training set. All the k-space data used for local training are undersampled using the SUNO mask predicted for the corresponding test scan, ensuring consistency between the sampling pattern and the locally adapted reconstructor.

Table V shows the reconstruction metrics for SUNO-Global and SUNO-Local on the fastMRI multi-coil knee dataset at $4\times$ and $8\times$ acceleration using the MoDL reconstructor. We observe that SUNO-Local provides additional improvements over SUNO-Global in some cases, particularly at lower acceleration factors, thus indicating the benefit of including scan-adaptive reconstruction combined with scan-adaptive sampling.

E. Lesion-Focused Evaluation With fastMRI+

To better evaluate reconstruction quality in regions containing pathologies, we used the publicly available fastMRI+ dataset [71] that provides expert-labeled bounding boxes for common abnormalities aligned with the original fastMRI dataset [64]. We applied the proposed SUNO masks and baseline masks to the knee k-space data at $4\times$ and $8\times$ acceleration factors. For evaluations, we used the MoDL reconstruction network trained on the original fastMRI dataset [64]. We computed NRMSE, SSIM, and PSNR over the full image to quantify reconstruction accuracy and assess signal fidelity across the entire anatomy. Table VI summarizes the results for $4\times$ and $8\times$ acceleration. The NRMSE of the reconstructed images obtained using all the masks was averaged over 115 testing images. SUNO achieved the lowest NRMSE at $4\times$ acceleration, outperforming other sampling patterns and getting an improved reconstruction of knee pathologies and lesions. At $8\times$, BASS achieved the best performance on this set, though SUNO remained competitive with lower NRMSE compared to other baselines.

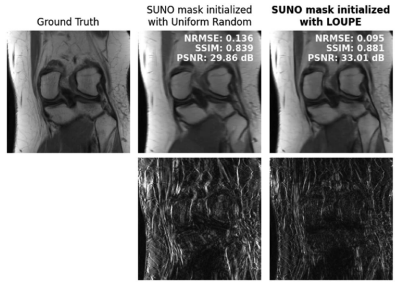

Fig. 9. Comparing reconstructed images using SUNO masks initialized from uniform random and LOUPE masks at $8\times$ acceleration factor.

F. Ablation Study - Convergence and Choice of Parameters for the Sampling Optimization Algorithm

In this section, we show the effect of changing different parameters for running the ICD sampling optimization (Algorithm 1) on the optimized SUNO masks for the fastMRI multi-coil knee dataset.

1) Effect of Initialization: In this section, we explore the effect of changing the initial mask used for the sampling pattern optimization - uniform random and LOUPE [47] masks. The algorithm, when started with a particular mask and given a choice of reconstruction method and loss used, could give different solutions. Table VII lists the performance metrics for the images reconstructed using SUNO masks optimized from a) uniform random mask and b) LOUPE mask with the MoDL reconstruction network. Fig. 9 shows one such example of the reconstructed images obtained from SUNO masks initialized using LOUPE and uniform random masks. From the results, we observe that the sampling optimization initialized with the LOUPE mask results in a better reconstruction compared to when it is initialized with a uniform random mask. Since the LOUPE mask is already optimized for multiple training scans (population adaptive), it acts as a better initial point for starting the sampling optimization. The algorithm further optimizes the LOUPE mask for scan-specific details, hence, we get better performance with it compared to LOUPE on test scans.

2) Effect of Reconstruction Method: This section shows the effect of the reconstruction method used inside the Algorithm 1 on the quality of optimized SUNO masks. The algorithm works for any choice of reconstruction method, e.g., compressed sensing (CS) or a pre-trained deep learning model (e.g., U-Net, MoDL, or E2E-VarNet [25], [26]). In this paper, we show masks optimized using two such methods - U-Net and MoDL and

TABLE V
COMPARISON OF SUNO WITH GLOBALLY TRAINED RECONSTRUCTION (SUNO-GLOBAL) AND LOCAL NEIGHBOR-ADAPTIVE RECONSTRUCTION (SUNO-LOCAL) ON THE FASTMRI MULTI-COIL KNEE DATASET USING THE MODL RECONSTRUCTOR. VALUES ARE REPORTED AS MEAN ± STANDARD DEVIATION OVER THE TEST SET.

	4×			8×		
Method	NRMSE ↓	SSIM ↑	PSNR ↑	NRMSE ↓	SSIM ↑	PSNR ↑
SUNO-Global	0.114 ± 0.046	0.940 ± 0.029	31.74 ± 2.85	0.162 ± 0.065	0.801 ± 0.068	28.66 ± 2.61
SUNO-Local	**0.110 ± 0.045**	**0.941 ± 0.029**	**32.07 ± 2.83**	**0.160 ± 0.066**	**0.803 ± 0.067**	**28.82 ± 2.66**

TABLE VI
MEAN NRMSE VALUES OVER THE RECONSTRUCTED IMAGES EVALUATED OVER THE FASTMRI+ TEST SET AT 4× AND 8× UNDERSAMPLING. LOWER VALUES INDICATE BETTER RECONSTRUCTION QUALITY.

Acceleration	LF	Uniform Random	VDPD	Equispaced	SeqMRI	LOUPE	BASS	SUNO-Global
4×	0.144	0.152	0.147	0.149	0.128	0.128	0.130	**0.128**
8×	0.207	0.240	0.183	0.225	0.188	0.186	**0.177**	0.182

TABLE VII
MEAN RECONSTRUCTION METRICS FOR MASKS INITIALIZED WITH UNIFORM RANDOM AND LOUPE AT AN 8× ACCELERATION FACTOR, EVALUATED OVER 50 TEST CASES. INITIALIZING WITH LOUPE RESULTS IN IMPROVED RECONSTRUCTION QUALITY.

Initial Mask Chosen	NRMSE ↓	SSIM ↑	PSNR ↑
Uniform Random	0.164	0.896	28.45
LOUPE	**0.142**	**0.903**	**29.78**

TABLE VIII
COMPUTATION TIME (MINUTES) FOR ONE PASS OF ALGORITHM 1 (OFFLINE) USING U-NET AND MODL RECONSTRUCTORS AT 4× AND 8× ACCELERATION. EXPERIMENTS WERE RUN ON AN NVIDIA RTX A5000 GPU WITH 24GB RAM.

Reconstructor Used	4× (min)	8× (min)
U-Net	25.3	13.3
MoDL	52.1	28.6

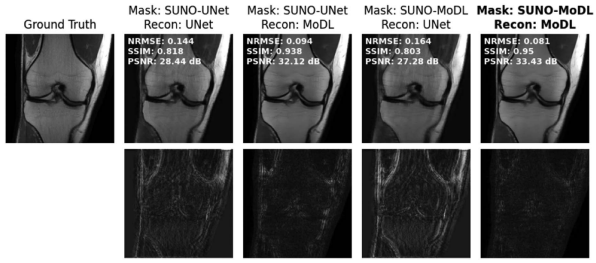

Fig. 10. Comparison of reconstructed images from masks optimized using 1) U-Net and 2) MoDL as the reconstruction model. For each mask, the reconstructed images using both the U-Net and MoDL networks is shown.

compare the reconstructed images using these masks. Fig. 10 shows the U-Net and MoDL reconstructed images using two optimized masks: one that used U-Net as the reconstruction model in the sampling optimization algorithm and the other with MoDL. The figure shows that we get the best reconstruction when a better reconstructor (i.e., MoDL network) is used both as the reconstruction model inside the sampling optimization and as the final reconstructor method.

G. Computational Cost of Proposed Approaches

This section discusses the time complexity of our proposed algorithms: 1) the sampling optimization algorithm and 2) the nearest neighbor search.

1) Complexity of Algorithm 1: In this section, we evaluate the effect of different parameters on the runtime of our proposed scan-adaptive sampling pattern optimization algorithm. Since our algorithm learns a unique mask for each training scan and slice, an important aspect to consider is the overall computational complexity. This makes training time and resource requirements an important practical consideration, especially for large datasets.

At each update of ICD, each movable line has $(N_y - B)$ candidate positions, where N_y and B denote the total number of phase encoding lines and the total sampling budget, respectively. Therefore across m moveable lines (where $m = B - c$, with c denoting the number of fixed lines in the center) and N_{iter} iterations, the computational cost of ICD sampling optimization is

$$\mathcal{O}(N_{iter}\, m\, (N_y - B))\,,$$

which is linear in N_{iter} and approximately linear in m when $N_y \gg m$.

Some of the parameters affecting runtime for the Algorithm 1 are the reconstruction method that is run repeatedly while moving sampling lines or phase encodes in the mask and the underlying undersampling factor. Table VIII shows the dependence of the runtime on both these parameters. It is clear from the table that the sampling optimization algorithm using a U-Net reconstruction model results in a lower runtime compared to running the algorithm using a MoDL reconstructor. This is because the MoDL reconstruction network uses multiple unrollings of the denoiser and the CG block [29]. These empirical observations are consistent with the theoretical scaling described above.

TABLE IX
TIME TAKEN (IN SECONDS) FOR NEAREST NEIGHBOR MASK SELECTION AND RECONSTRUCTION NETWORK INFERENCE

Procedure	Time (s)
Nearest Neighbor Mask Selection	0.85
Inference	1.53

2) Cost of Nearest Neighbor Search: In this section, we discuss the time complexity of the nearest neighbor search used for mask selection at test time. After the initial low-frequency k-space lines are acquired, we compute distances between the test scan and all training scans and select the SUNO mask associated with the closest neighbor. The chosen mask is then used to acquire the remaining k-space lines, followed by reconstruction with the trained network.

Table IX reports the time required for nearest neighbor mask selection and for a single forward pass of the reconstruction network (inference). These steps introduce only a small computational overhead relative to the overall scan and reconstruction pipeline.

V. DISCUSSION

We proposed a novel way of learning scan-adaptive Cartesian undersampling patterns for multi-coil MRI. The proposed method demonstrated better accuracy than population-based 1D Cartesian undersampling patterns in terms of NRMSE, SSIM, and PSNR, as well as improved visual quality at $4\times$ and $8\times$ acceleration factors. Zoomed-in images highlight improved feature preservation in reconstructions using SUNO masks compared to other baselines. The method was tested on knee and brain datasets, indicating generalization across anatomies.

Similar to the greedy algorithm in prior work [42], the sampling optimization algorithm can be used along with any choice of reconstruction method and the loss metric, giving freedom in designing sampling patterns for different anatomies and different acceleration factors. At test time, a nearest neighbor search was used to predict the pattern from the dictionary of learned patterns. Furthermore, we also evaluated the effect of having local neighbor-adaptive reconstruction, which can provide further improvements over a globally trained reconstruction. The current experiments used a single nearest-neighbor approach for mask selection. While alternative approaches such as k-nearest neighbor aggregation or learned models could be explored, a systematic evaluation of these techniques was not performed in this work. The nearest-neighbor approach may be susceptible to outliers as well, and future research in this direction could explore more robust selection approaches.

Our proposed scan-adaptive sampling algorithm is influenced by the choice of initial mask. A population-adaptive mask, such as LOUPE, acts as a better initial point and leads to improved reconstructions compared to a uniform random mask, as the algorithm performs local line-by-line updates rather than large-scale reconfigurations. Future work could explore using multiple initializations or randomized perturbations during training to reduce dependence on a single starting mask.

We observed that certain small anatomical structures were not well recovered in any of the $8\times$ accelerated reconstructions, regardless of the method used. Similarly, in the brain, small structures sometimes appeared distorted or hallucinated in the reconstructed images. These limitations highlight that although the scan-adaptive SUNO masks improve global metrics and preserve most of the anatomical details, recovering some small, low-contrast features remains challenging. In the knee, these errors may be due to the need for higher frequencies to capture these small structures, which the learned masks do not fully cover currently. Similarly, in the brain, undersampling combined with the reconstruction network can introduce small spurious features. Optimizing scan-adaptive masks with ROI-specific loss functions may enable better recovery of such fine structures and represents an important direction for future work.

In addition to quantitative performance, we analyzed the characteristics of the scan-adaptive undersampling patterns across different subjects. We observed substantial variation in the high-frequency sampling locations across slices and subjects. While part of this variation may arise from random initialization of the masks for each scan, much of it reflects adaptation to individual anatomy and image content. This combination of shared structure and individualized detail highlights the potential advantages of scan-adaptive sampling over fixed, population-based designs. At the same time, the broader question of whether scan-adaptive sampling is inherently superior to population-based sampling techniques remains open in the deep learning setting. For instance, under certain reconstruction objectives and regularization choices, population-based methods such as LOUPE can outperform some scan-adaptive approaches. To address this, we included recent state-of-the-art human-designed (VDPD) and population-based (BASS) baselines, and our results show that SUNO consistently outperformed them in most cases. Nevertheless, broader benchmarking across architectures and datasets will be needed to fully resolve this important question.

While our experiments used 1D undersampling adaptations of VDPD and BASS to remain consistent with the 2D Cartesian acquisitions studied here, we acknowledge that fully 2D undersampling implementations of these methods for 3D acquisitions may provide further insights. Extending SUNO and such baselines beyond 1D undersampling constitutes an important direction for future work. Though the larger search space in higher dimensions makes these extensions more computationally demanding, this could potentially be alleviated using randomized search techniques. Recent work, such as AutoSamp [52], has advanced the design of population-based sampling techniques through more sophisticated optimization and learning formulations. Adapting and comparing such approaches within the Cartesian acquisition setting studied here would help place scan-adaptive methods like SUNO in a broader context of sampling design.

A drawback of the current method is the time-consuming process of learning scan-adaptive sampling patterns on the whole training set. More work is required to make the optimization process efficient and faster, to make this approach more feasible. However, since this sampling optimization is part of the offline

training module, it does not affect the acquisition and sampling prediction at test time, which is 0.85 seconds in our experiments.

VI. Conclusion

In this work, we proposed a novel MRI sampling prediction algorithm for multi-coil MRI that estimates a collection of scan-adaptive sampling patterns and a reconstruction network trained on those patterns alternatingly, at training time. The proposed algorithm was validated on the publicly available fastMRI knee and brain datasets and demonstrated better reconstruction accuracy than the currently used Cartesian undersampling patterns. This study demonstrated the advantages of employing scan-adaptive masks by providing evidence that they are more effectively tailored to individual patients than population-adaptive masks. We also showed the dependence of the learned sampling patterns on acceleration factors, the initialization of the sampling algorithm, and the reconstruction method used. Future work will include employing deep image prior or other scan-adaptive MRI reconstructions in our framework, extending the approach to cardiac MRI, and/or predicting sparse views for X-ray CT reconstruction.

Acknowledgment

The authors would like to acknowledge Dr. Maryam Sayadi, Michigan State University for her inputs throughout the project. The authors also acknowledge Evan Bell and Shijun Liang from Michigan State University and Zhishen Huang from Amazon Inc. for useful discussions.

References

[1] Z. Liang and P. C. Lauterbur, *Principles of Magnetic Resonance Imaging*. Bellingham, WA, USA: SPIE Optical Engineering Press Belllingham, 2000.
[2] M. A. Bernstein, K. F. King, and X. J. Zhou, *Handbook of MRI Pulse Sequences*. Amesterdam, The Netherlands: Elsevier, 2004.
[3] J. Tsao, "Ultrafast imaging: Principles, pitfalls, solutions, and applications," *J. Magn. Reson. Imag.*, vol. 32, no. 2, pp. 252–266, 2010.
[4] K. P. Pruessmann, M. Weiger, M. B. Scheidegger, and P. Boesiger, "SENSE: Sensitivity encoding for fast MRI," *Magn. Reson. Med.*, vol. 42, no. 5, pp. 952–962, 1999.
[5] M. A. Griswold et al., "Generalized autocalibrating partially parallel acquisitions (GRAPPA)," *Magn. Reson. Med.*, vol. 47, no. 6, pp. 1202–1210, 2002.
[6] L. Ying and Z.-P. Liang, "Parallel MRI using phased array coils," *IEEE Signal Process. Mag.*, vol. 27, no. 4, pp. 90–98, Jul. 2010.
[7] A. Deshmane, V. Gulani, M. A. Griswold, and N. Seiberlich, "Parallel MR imaging," *J. Magn. Reson. Imag.*, vol. 36, no. 1, pp. 55–72, 2012.
[8] D. L. Donoho, "Compressed sensing," *IEEE Trans. Inf. Theory*, vol. 52, no. 4, pp. 1289–1306, Apr. 2006.
[9] M. Lustig, D. Donoho, and J. M. Pauly, "Sparse MRI: The application of compressed sensing for rapid MR imaging," *Magn. Reson. Med.*, vol. 58, no. 6, pp. 1182–1195, 2007.
[10] M. Lustig, D. L. Donoho, J. M. Santos, and J. M. Pauly, "Compressed sensing MRI," *IEEE Signal Process. Mag.*, vol. 25, no. 2, pp. 72–82, Mar. 2008.
[11] S. Ravishankar and Y. Bresler, "MR image reconstruction from highly undersampled k-space data by dictionary learning," *IEEE Trans. Med. Imag.*, vol. 30, no. 5, pp. 1028–1041, May 2011.
[12] S. G. Lingala and M. Jacob, "Blind compressive sensing dynamic MRI," *IEEE Trans. Med. Imag.*, vol. 32, no. 6, pp. 1132–1145, Jun. 2013.
[13] X. Qu, Y. Hou, F. Lam, D. Guo, J. Zhong, and Z. Chen, "Magnetic resonance image reconstruction from undersampled measurements using a patch-based nonlocal operator," *Med. Image Anal.*, vol. 18, no. 6, pp. 843–856, 2014.
[14] Z. Zhan, J.-F. Cai, D. Guo, Y. Liu, Z. Chen, and X. Qu, "Fast multiclass dictionaries learning with geometrical directions in MRI reconstruction," *IEEE Trans. Biomed. Eng.*, vol. 63, no. 9, pp. 1850–1861, Sep. 2015.
[15] S. Ravishankar and Y. Bresler, "Learning sparsifying transforms," *IEEE Trans. Signal Process.*, vol. 61, no. 5, pp. 1072–1086, Mar. 2013.
[16] S. Ravishankar, J. C. Ye, and J. A. Fessler, "Image reconstruction: From sparsity to data-adaptive methods and machine learning," *Proc. IEEE*, vol. 108, no. 1, pp. 86–109, Jan. 2020.
[17] Y. Yang, J. Sun, H. Li, and Z. Xu, "Deep ADMM-Net for compressive sensing MRI," in *Proc. Adv. Neural Inf. Process. Syst.*, vol. 29, 2016.
[18] Y. Yang, J. Sun, H. Li, and Z. Xu, "ADMM-Net: A deep learning approach for compressive sensing MRI," 2017, *arXiv:1705.06869*.
[19] J. Zhang and B. Ghanem, "ISTA-Net: Interpretable optimization-inspired deep network for image compressive sensing," in *Proc. IEEE Conf. Comput. Vis. Pattern Recognit.*, 2018, pp. 1828–1837.
[20] O. Ronneberger, P. Fischer, and T. Brox, "U-net: Convolutional networks for biomedical image segmentation," in *Proc. Int. Conf. Med. Image Comput. Comput.- Assist. Intervention*, 2015, pp. 234–241.
[21] C. M. Hyun, H. P. Kim, S. M. Lee, S. Lee, and J. K. Seo, "Deep learning for undersampled MRI reconstruction," *Phys. Med. Biol.*, vol. 63, no. 13, 2018, Art. no. 135007.
[22] B. Zhu, J. Z. Liu, S. F. Cauley, B. R. Rosen, and M. S. Rosen, "Image reconstruction by domain-transform manifold learning," *Nature*, vol. 555, no. 7697, pp. 487–492, 2018.
[23] G. Wang, J. C. Ye, K. Mueller, and J. A. Fessler, "Image reconstruction is a new frontier of machine learning," *IEEE Trans. Med. Imag.*, vol. 37, no. 6, pp. 1289–1296, Jun. 2018.
[24] F. Knoll et al., "Deep-learning methods for parallel magnetic resonance imaging reconstruction: A survey of the current approaches, trends, and issues," *IEEE Signal Process. Mag.*, vol. 37, no. 1, pp. 128–140, Jan. 2020.
[25] K. Hammernik et al., "Learning a variational network for reconstruction of accelerated MRI data," *Magn. Reson. Med.*, vol. 79, no. 6, pp. 3055–3071, 2018.
[26] A. Sriram et al., "End-to-end variational networks for accelerated MRI reconstruction," in *Proc. 23rd Int. Conf. Med. Image Comput. Comput. Assist. Intervention*, 2020, pp. 64–73.
[27] M. Mardani et al., "Deep generative adversarial neural networks for compressive sensing MRI," *IEEE Trans. Med. Imag.*, vol. 38, no. 1, pp. 167–179, Jan. 2019, doi: 10.1109/TMI.2018.2858752.
[28] G. Yang et al., "DAGAN: Deep de-aliasing generative adversarial networks for fast compressed sensing MRI reconstruction," *IEEE Trans. Med. Imag.*, vol. 37, no. 6, pp. 1310–1321, Jun. 2018.
[29] H. K. Aggarwal, M. P. Mani, and M. Jacob, "MoDL: Model-based deep learning architecture for inverse problems," *IEEE Trans. Med. Imag.*, vol. 38, no. 2, pp. 394–405, Feb. 2019.
[30] H. K. Aggarwal and M. Jacob, "J-MoDL: Joint model-based deep learning for optimized sampling and reconstruction," *IEEE J. Sel. Topics Signal Process.*, vol. 14, no. 6, pp. 1151–1162, Oct. 2020.
[31] U. Gamper, P. Boesiger, and S. Kozerke, "Compressed sensing in dynamic MRI," *Magn. Reson. Med.*, vol. 59, no. 2, pp. 365–373, 2008.
[32] J. P. Haldar, D. Hernando, and Z.-P. Liang, "Compressed-sensing MRI with random encoding," *IEEE Trans. Med. Imag.*, vol. 30, no. 4, pp. 893–903, Apr. 2011.
[33] R. Bridson, "Fast Poisson disk sampling in arbitrary dimensions," in *Proc. ACM SIGGRAPH Sketches*, 2007, Art. no. 22.
[34] M. Lustig and J. M. Pauly, "SPIRiT: Iterative self-consistent parallel imaging reconstruction from arbitrary k-space," *Magn. Reson. Med.*, vol. 64, no. 2, pp. 457–471, 2010.
[35] E. Levine, B. Daniel, S. Vasanawala, B. Hargreaves, and M. Saranathan, "3D cartesian MRI with compressed sensing and variable view sharing using complementary poisson-disc sampling," *Magn. Reson. Med.*, vol. 77, no. 5, pp. 1774–1785, 2017.
[36] S. Ravishankar and Y. Bresler, "Adaptive sampling design for compressed sensing MRI," in *Proc. 2011 Annu. Int. Conf. IEEE Eng. Med. Biol. Soc.*, 2011, pp. 3751–3755.
[37] F. Knoll, C. Clason, C. Diwoky, and R. Stollberger, "Adapted random sampling patterns for accelerated MRI," *Magn. Reson. Materials Phys., Biol. Med.*, vol. 24, pp. 43–50, 2011.
[38] J. Vellagoundar and R. R. Machireddy, "A robust adaptive sampling method for faster acquisition of MR images," *Magn. Reson. Imag.*, vol. 33, no. 5, pp. 635–643, 2015.
[39] Y. Zhang, B. S. Peterson, G. Ji, and Z. Dong, "Energy preserved sampling for compressed sensing MRI," *Comput. Math. Methods Med.*, vol. 2014, no. 1, 2014, Art. no. 546814.

[40] J. P. Haldar and D. Kim, "OEDIPUS: An experiment design framework for sparsity-constrained MRI," *IEEE Trans. Med. Imag.*, vol. 38, no. 7, pp. 1545–1558, Jul. 2019.
[41] M. Seeger, H. Nickisch, R. Pohmann, and B. Schölkopf, "Optimization of k-space trajectories for compressed sensing by bayesian experimental design," *Magn. Reson. Med.*, vol. 63, no. 1, pp. 116–126, 2010.
[42] B. Gözcü et al., "Learning-based compressive MRI," *IEEE Trans. Med. Imag.*, vol. 37, no. 6, pp. 1394–1406, Jun. 2018.
[43] B. Gözcü, T. Sanchez, and V. Cevher, "Rethinking sampling in parallel MRI: A data-driven approach," in *Proc. 27th Eur. Signal Process. Conf.*, 2019, pp. 1–5.
[44] T. Sanchez et al., "Scalable learning-based sampling optimization for compressive dynamic MRI," in *Proc. 2020 IEEE Int. Conf. Acoust., Speech Signal Process.*, 2020, pp. 8584–8588.
[45] M. V. Zibetti, G. T. Herman, and R. R. Regatte, "Fast data-driven learning of parallel MRI sampling patterns for large scale problems," *Sci. Rep.*, vol. 11, no. 1, 2021, Art. no. 19312.
[46] M. V. W. Zibetti, F. Knoll, and R. R. Regatte, "Alternating learning approach for variational networks and undersampling pattern in parallel MRI applications," *IEEE Trans. Comput. Imag.*, vol. 8, pp. 449–461, 2022.
[47] C. D. Bahadir, A. Q. Wang, A. V. Dalca, and M. R. Sabuncu, "Deep-learning-based optimization of the under-sampling pattern in MRI," *IEEE Trans. Comput. Imag.*, vol. 6, pp. 1139–1152, 2020.
[48] J. Zhang et al., "Extending LOUPE for k-space under-sampling pattern optimization in multi-coil MRI," in *Proc. 3rd Int. Workshop, Mach. Learn. Med. Image Reconstruction*, 2020, pp. 91–101.
[49] F. Sherry et al., "Learning the sampling pattern for MRI," *IEEE Trans. Med. Imag.*, vol. 39, no. 12, pp. 4310–4321, Dec. 2020.
[50] T. Yin, Z. Wu, H. Sun, A. V. Dalca, Y. Yue, and K. L. Bouman, "End-to-end sequential sampling and reconstruction for MRI," in *Proc. Mach. Learn. Health*, vol. 158, 2021, pp. 261–281.
[51] Z. Huang and S. Ravishankar, "Single-pass object-adaptive data undersampling and reconstruction for MRI," *IEEE Trans. Comput. Imag.*, vol. 8, pp. 333–345, 2022.
[52] C. Alkan, M. Mardani, C. Liao, Z. Li, S. S. Vasanawala, and J. M. Pauly, "AutoSamp: Autoencoding k-space sampling via variational information maximization for 3-D MRI," *IEEE Trans. Med. Imag.*, vol. 44, no. 1, pp. 270–283, Jan. 2025.
[53] T. Weiss, O. Senouf, S. Vedula, O. Michailovich, M. Zibulevsky,, and A. Bronstein, "PILOT: Physics-informed learned optimized trajectories for accelerated MRI," *Mach. Learn. Biomed. Imag.*, vol. 123, Apr. 2021, doi: 10.59275/j.melba.2021-1a1f.
[54] C. Lazarus et al., "Sparkling: Variable-density k-space filling curves for accelerated T2∗-weighted MRI," *Magn. Reson. Med.*, vol. 81, no. 6, pp. 3643–3661, 2019.
[55] G. R. Chaithya, P. Weiss, G. Daval-Frérot, A. Massire, A. Vignaud, and P. Ciuciu, "Optimizing full 3D sparkling trajectories for high-resolution magnetic resonance imaging," *IEEE Trans. Med. Imag.*, vol. 41, no. 8, pp. 2105–2117, Aug. 2022.
[56] G. Wang, T. Luo, J. Nielsen, D. C. Noll, and J. A. Fessler, "B-spline parameterized joint optimization of reconstruction and k-space trajectories (BJORK) for accelerated 2D MRI," *IEEE Trans. Med. Imag.*, vol. 41, no. 9, pp. 2318–2330, Sep. 2022.
[57] Z. Ramzi, C. G R, J.-L. Starck, and P. Ciuciu, "NC-PDNet: A density-compensated unrolled network for 2D and 3D non-cartesian MRI reconstruction," *IEEE Trans. Med. Imag.*, vol. 41, no. 7, pp. 1625–1638, Jul. 2022.
[58] G. Wang, J. F. Nielsen, J. A. Fessler, and D. C. Noll, "Stochastic optimization of three-dimensional non-cartesian sampling trajectory," *Magn. Reson. Med.*, vol. 90, no. 2, pp. 417–431, 2023.
[59] L. Pineda, S. Basu, A. Romero, R. Calandra, and M. Drozdzal, "Active MR k-space sampling with reinforcement learning," in *Proc. 23rd Int. Conf., Med. Image Comput. Comput. Assist. Intervention*, Lima, Peru, 2020, pp. 23–33.
[60] T. Bakker, H. van Hoof, and M. Welling, "Experimental design for MRI by greedy policy search," in *Proc. Adv. Neural Inf. Process. Syst.*, 2020, vol. 33, pp. 18954–18966.
[61] Z. Wang, A. C. Bovik, H. R. Sheikh, and E. P. Simoncelli, "Image quality assessment: From error visibility to structural similarity," *IEEE Trans. Image Process.*, vol. 13, no. 4, pp. 600–612, Apr. 2004.
[62] S. Gautam, A. Li, and S. Ravishankar, "Patient-adaptive and learned MRI data undersampling using neighborhood clustering," in *Proc. 2024 IEEE Int. Conf. Acoust., Speech Signal Process.*, 2024, pp. 2081–2085.
[63] B. Yaman, S. A. Hosseini, and M. Akcakaya, "Zero-shot self-supervised learning for MRI reconstruction," in *Proc. Int. Conf. Learn. Representations*, 2022.
[64] J. Zbontar et al., "fastMRI: An open dataset and benchmarks for accelerated MRI," 2018, *arXiv:1811.08839*.
[65] F. Knoll et al., "fastMRI: A publicly available raw k-space and DICOM dataset of knee images for accelerated MR image reconstruction using machine learning," *Radiol., Artif. Intell.*, vol. 2, no. 1, 2020, Art. no. e190007.
[66] M. Uecker et al., "ESPIRiT — An eigenvalue approach to autocalibrating parallel MRI: Where SENSE meets GRAPPA," *Magn. Reson. Med.*, vol. 71, no. 3, pp. 990–1001, 2014.
[67] Y. Bengio, N. Léonard, and A. Courville, "Estimating or propagating gradients through stochastic neurons for conditional computation," 2013, *arXiv:1308.3432*.
[68] S. Yu, B. Park, and J. Jeong, "Deep iterative down-up CNN for image denoising," in *Proc. IEEE/CVF Conf. Comput. Vis. Pattern Recognit. Workshops*, 2019, pp. 2095–2103.
[69] D. P. Kingma and J. Ba, "Adam: A method for stochastic optimization," 2014, *arXiv:1412.6980*.
[70] S. Liang, A. Lahiri, and S. Ravishankar, "Adaptive local neighborhood-based neural networks for MR image reconstruction from undersampled data," *IEEE Trans. Comput. Imag.*, vol. 10, pp. 1235–1249, 2024.
[71] R. Zhao et al., "fastMRI, clinical pathology annotations for knee and brain fully sampled magnetic resonance imaging data," *Sci. Data*, vol. 9, no. 1, 2022, Art. no. 152.

Scan-Adaptive MRI Undersampling Using Neighbor-Based Optimization (SUNO): Supplementary Material

Siddhant Gautam, *Student Member, IEEE*, Angqi Li, Nicole Seiberlich, Jeffrey A. Fessler, *Fellow, IEEE*, and Saiprasad Ravishankar, *Senior Member, IEEE*

This supplementary material accompanies the main paper:

S. Gautam, A. Li, N. Seiberlich, J. A. Fessler, and S. Ravishankar, "Scan-Adaptive MRI Undersampling Using Neighbor-Based Optimization (SUNO)," accepted for publication in *IEEE Transactions on Computational Imaging*, 2026.

S1. Additional Examples of Scan-Adaptive Masks

To illustrate the variability of scan-adaptive sampling methods, Figure S1 shows two additional examples from different test scans from the fastMRI knee dataset [1]. For each scan, we show the fully sampled ground truth magnitude image, along with the SeqMRI [2] and the SUNO masks.

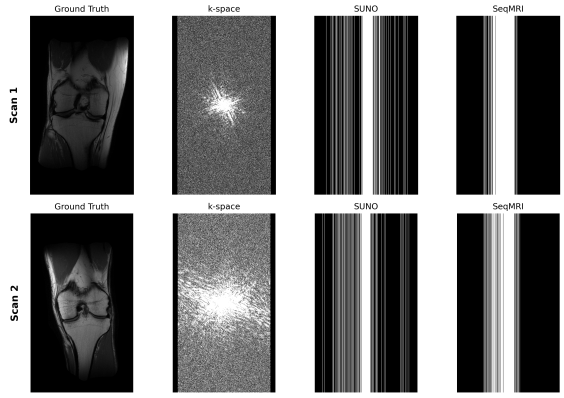

Fig. S1: Representative examples of scan-adaptive sampling masks from the fastMRI knee dataset, showing (from left to right): ground truth magnitude image, fully sampled k-space (to illustrate energy distribution), scan-adaptive SUNO mask, and scan-adaptive SeqMRI mask. These examples illustrate the variability of scan-adaptive methods across subjects, and suggest that differences across scans may be linked to k-space energy distribution.

S2. Additional Results on fastMRI+ Dataset

We performed additional experiments on the fastMRI+ knee dataset with pathological annotations at 4× and 8× accelerations [3]. Here, we additionally report SSIM and PSNR metrics for this dataset. Table S1 summarizes the global reconstruction metrics, while Figure S2 shows representative reconstructions with zoomed-in views of annotated regions of interest (ROIs). These results further demonstrate that SUNO achieves better reconstruction quality compared to baseline sampling masks at 4×. At 8×, SUNO remains competitive, but BASS achieves slightly better metrics, including better reconstruction of clinically relevant pathological regions.

Method	4×	8×
LF	0.144 / 0.840 / 30.31	0.207 / 0.752 / 27.26
Random Uniform	0.152 / 0.815 / 29.53	0.240 / 0.726 / 25.53
VDPD	0.147 / 0.823 / 29.88	0.184 / 0.757 / 28.01
Equispaced	0.149 / 0.827 / 29.81	0.225 / 0.733 / 26.11
SeqMRI	0.129 / 0.855 / 31.09	0.188 / 0.779 / 27.71
LOUPE	0.128 / 0.853 / 31.13	0.186 / 0.776 / 28.05
BASS	0.130 / 0.846 / 31.16	**0.177 / 0.781 / 28.16**
SUNO-Global	0.128 / 0.857 / 31.32	0.182 / 0.779 / 28.10
SUNO-Local	**0.127 / 0.860 / 31.41**	0.180 / 0.780 / 28.13

TABLE S1: Global reconstruction performance on the fastMRI+ knee dataset at 4× and 8× acceleration. Values reported as (NRMSE, SSIM, PSNR). Lower NRMSE and higher SSIM/PSNR indicate better reconstruction quality.

References

[1] J. Zbontar, F. Knoll, A. Sriram, T. Murrell, Z. Huang, M.J. Muckley, A. Defazio, R. Stern, P. Johnson, M. Bruno, et al., "fastMRI: An open dataset and benchmarks for accelerated MRI," *arXiv preprint arXiv:1811.08839*, 2018.

[2] T. Yin, Z. Wu, H. Sun, A.V. Dalca, Y. Yue, and K.L. Bouman, "End-to-end sequential sampling and reconstruction for MR imaging," in *Proceedings of the Machine Learning for Health Conference*, 2021.

[3] R. Zhao, B. Yaman, Y. Zhang, R. Stewart, A. Dixon, F. Knoll, Z. Huang, Y. W. Lui, M. S. Hansen, and M. P. Lungren, "fastMRI+, clinical pathology annotations for knee and brain fully sampled magnetic resonance imaging data," *Scientific Data*, vol. 9, no. 1, pp. 152, 2022.

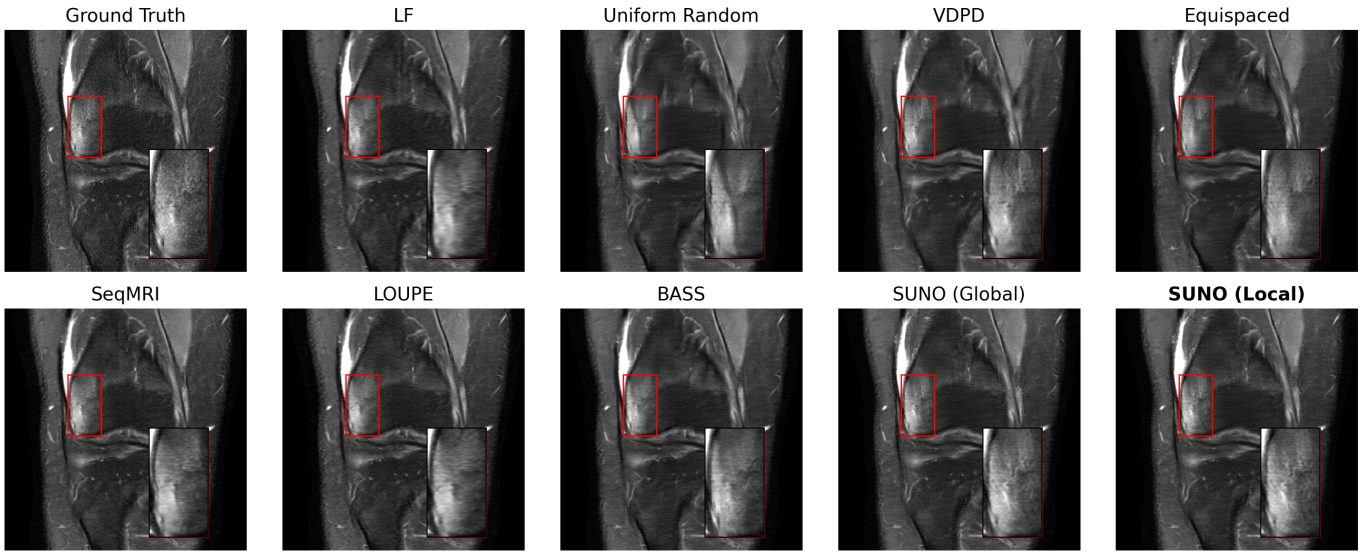

(a)

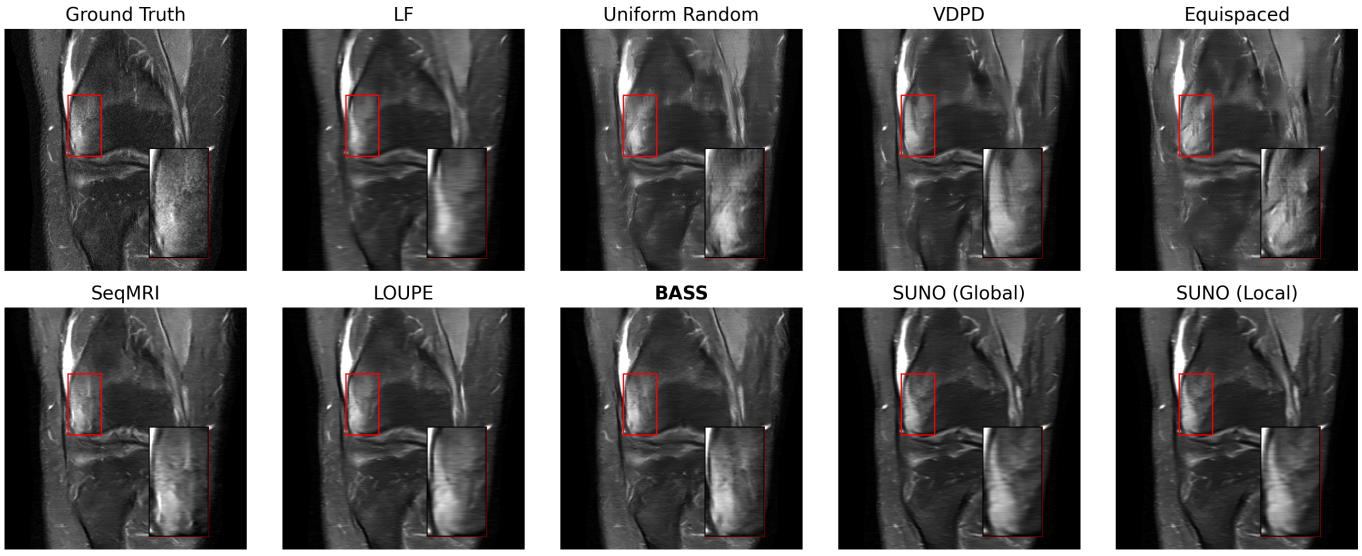

(b)

Fig. S2: Representative reconstructions from the fastMRI+ knee dataset at (a) 4× and (b) 8× acceleration. Each panel shows the ground truth (GT), baseline reconstructions, and SUNO results with zoomed-in ROI views. At 4×, SUNO achieves the best overall reconstruction quality and preserves pathological details more faithfully. At 8×, SUNO remains competitive but BASS achieves slightly better global metrics, consistent with Table S1.